Available online at www.sciencedirect.com

SciVerse ScienceDirect

journal homepage: www.elsevier.com/locate/he

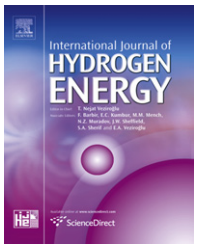

Optimization of purge cycle for dead-ended anode fuel cell operation

Jixin Chen [a,*], Jason B. Siegel [a], Anna G. Stefanopoulou [a], James R. Waldecker [b]

[a] Department of Mechanical Engineering, University of Michigan, 2350 Hayward St., Ann Arbor, MI 48109, USA
[b] Fuel Cell Stack Research, Research and Innovation Center, Ford Motor Company, Dearborn, MI 48121, USA

ARTICLE INFO

Article history:
Received 9 October 2012
Received in revised form
19 January 2013
Accepted 5 February 2013
Available online 9 March 2013

Keywords:
Dead-ended anode
Fuel cell optimization
Hydrogen loss
Carbon corrosion
Lifetime efficiency

ABSTRACT

Dead-Ended Anode (DEA) operation of Proton Exchange Membrane Fuel Cells (PEMFCs) yields a system with lower complexity and the potential to reduce system cost as fewer external components are required. Optimization of the purge interval and cycle duration, for a given operating power, can increase the fuel cell efficiency which depends on three interrelated objectives, namely, the hydrogen loss during the purge, the average voltage output between the purges, and the voltage decrease due to the carbon corrosion caused by hydrogen starvation over the lifetime of the DEA operation.

In advancing past results, this paper shows how the purge cycle can be optimized for better efficiency in DEA operation by considering the impact of carbon corrosion. For this optimization, a model capturing the liquid water and nitrogen accumulation in the anode is needed to accurately describe the evolution of corrosion rate and the amount of hydrogen wasted during the purge. The optimization process is first defining a target range of purge intervals based on the physical constraints of the actuator and the model-based prediction of the species concentration distributions. The search of optima is performed then by scanning the target domain to quantify the trade-off between wasted hydrogen and reducing the corrosion rate over a long time horizon.

1. Introduction

Dead-end anode (DEA) operation has been implemented and studied by several groups [1–3]. A DEA fuel cell is fed by dry hydrogen with regulated pressure at the anode inlet. Inlet pressure regulation ensures that the hydrogen inlet stoichiometry is exactly one during DEA operation and the channel pressure remains constant. A DEA fuel cell system, as shown in Fig. 1b, requires fewer auxiliary components when compared to the more traditional flow-through anode (FTA) shown in Fig. 1a. The flow-through operation with hydrogen flow control depends on a recirculation loop to maintain a high hydrogen utilization and enhanced convective transport, which requires hydrogen grade plumbing and hardware such as an ejector/blower and a water separator/demister [4]. These balance of plant (BOP) components add weight, volume, and expense to the system, although the necessity of anode humidifier has been gradually eliminated in the state-of-art fuel cell systems [4] as compared with those in the 2000s [5].

There are unfortunately other concerns with the DEA fuel cell system. During the DEA operation, nitrogen and liquid water accumulate in the anode channel, causing a gradual drop in cell voltage over time [6,7]. Purging of the anode channel recovers the voltage by removing the accumulated

* *Corresponding author*. Tel.: +1 (734) 615 8461.
E-mail address: jixinc@umich.edu (J. Chen).

0360-3199/$ – see front matter
http://dx.doi.org/10.1016/j.ijhydene.2013.02.022

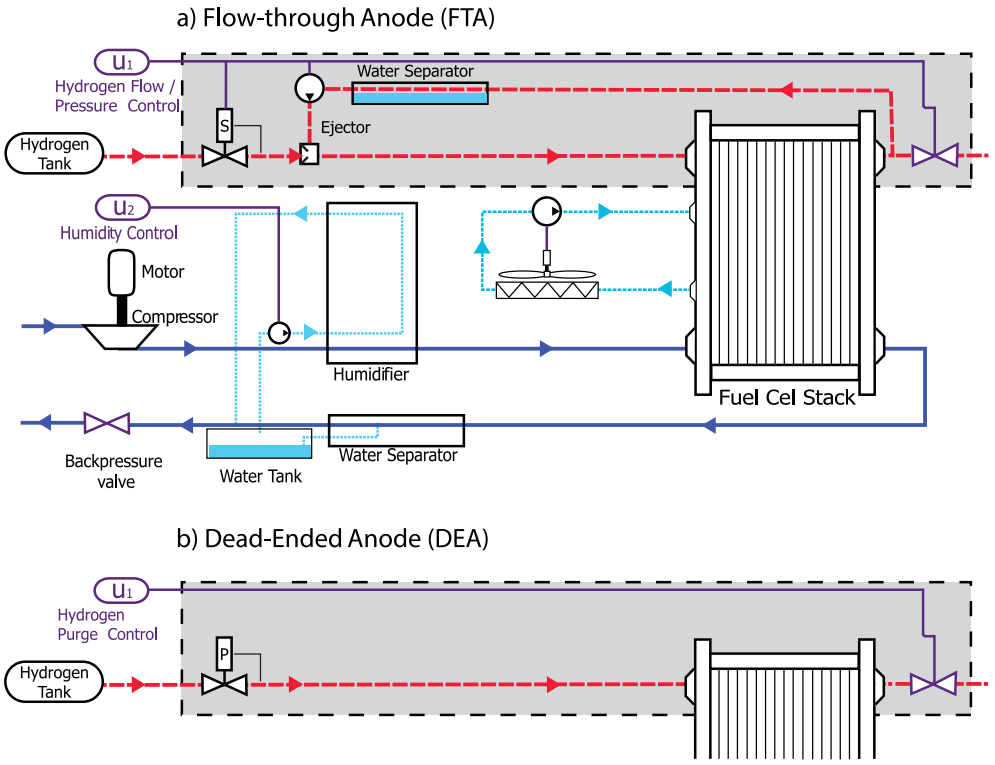

Fig. 1 – Schematic of fuel cell systems with flow-through anode versus dead-ended anode. DEA operation depends on upstream pressure regulation instead of mass flow control. If the purge interval is controlled with minimum hydrogen loss, there is less need for hydrogen re-circulation system. The DEA fuel cell system therefore features fewer auxiliary components and reduced system weight, volume and cost.

nitrogen and water. A cyclic voltage behavior can thus be observed when a periodic purge schedule is applied, as illustrated in Fig. 2.

If allowed to continue without purging, the accumulation of nitrogen and liquid water in the anode channel during DEA operation would lead to local fuel depletion or starvation, triggering corrosion of the carbon as catalyst support in the cathode. Cathode carbon corrosion is a concern because it causes irreversible loss of fuel cell voltage and decreases the stack lifetime. In our recent work [8] the spatio-temporal evolution of carbon corrosion rate due to the elevated cathode interfacial potential during DEA operation has been studied via simulation. In addition, the uneven local current and membrane water content during DEA operation may expedite membrane degradation including crack/tear, pin-hole and polymer decomposition [9,10]. The impact of degradation on cell terminal voltage and therefore efficiency over the entire lifetime of the cell, is an important consideration for purge scheduling. In this paper, we aim to elucidate the connection between purge scheduling, degradation and efficiency over the entire cell lifetime.

There are many prior publications in fuel cell optimization [11]. Some focus on the component design such as flow field [12,13] and electrode [14,15] and some on the operating schemes [16,17]. Usually, the objective of optimization is to maximize energy output or efficiency [18,19]. These prior works are based on flow-through operation of the fuel cell. For DEA operation, early works mainly focus on reducing hydrogen loss or increasing power output via optimization of a specific operating parameter. Hikita et al. [20] investigated the

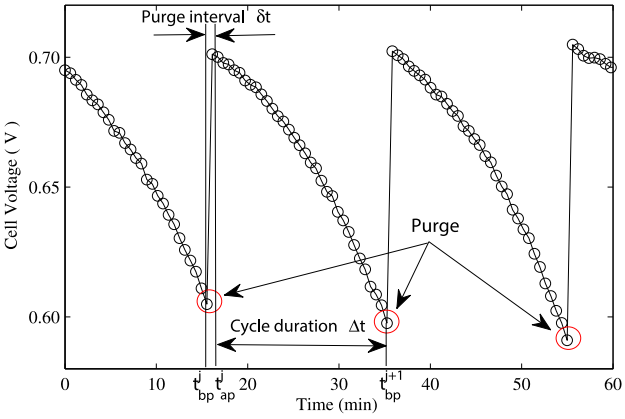

Fig. 2 – Representative voltage cycles during the galvanostatic DEA operation. t_{bp}^{j} is the end of the jth DEA cycle (the moment right before the jth purge) and t_{ap}^{j} is the beginning of the $(j+1)$th cycle (the moment right after the jth purge). Purge interval δt, which equals to $t_{ap}^{j} - t_{bp}^{j}$, is controlled by a solenoid valve downstream of the fuel cell anode. Cycle duration, Δt, is the amount of time between the end of the proceeding purge, t_{ap}^{j} and the start of the subsequent purge, t_{bp}^{j+1}. The accumulation of nitrogen and liquid water in the anode channel between purges is responsible for the recoverable voltage loss in a DEA cycle.

optimum humidification for a DEA cell according to current density, as well as the influence of operating pressure on the power generation characteristics. Dumercy et al. [21] developed a stack model to calculate the optimal purge frequency for a three-cell stack with DEA in order to achieve satisfactory power output. Himanen et al. [22] studied the influences of hydrogen pressures, humidification conditions and purge valve duty cycles on the performance of an anodic dead-end mode PEM fuel cell with free-breathing cathode. In a recent study of DEA operation by Choi et al. [23], hydrogen pulsation is utilized to reduce the vapor partial pressure in the anode, thereby minimizing the purge frequency and associated hydrogen loss. The dynamic performance of a stack with near-dead-ended anode in a vehicular drive system was modeled by Dehn et al. [24]. They found that an increase in anode pressure is beneficial for near-dead-ended anode operation and does not lower the efficiency of the fuel cell system. Yang and Shi [25] designed a six cell stack, with dead-ended anode and air-breathing cathode, to achieve uniform stack performance and high efficiency. Mokmeli and Asghari [26] investigated the proper purge time to achieve the minimum pressure fluctuations, minimum voltage loss and minimum hydrogen waste by mathematical modeling and analysis. Their work, however, does not focus on the cell efficiency in DEA operation. These early works aim to improve either the power output or the hydrogen loss; however, the connection between these two factors has not been studied thoroughly. Finally, the degradation of a stack with DEA, which is critical for automotive application, has not been investigated in these works.

The objective of this paper is to optimize the efficiency of a DEA fuel cell via purge scheduling while considering the performance degradation due to carbon corrosion. The optimization is performed on the purge interval and cycle duration shown in Fig. 2. Operating conditions such as current load also influence both fuel cell efficiency and degradation; however for a portable application these conditions are usually determined by the power requirement and thus considered as parameters in this study. The optimization is performed based on the simulation results using a validated two-phase, 1+1D model, which gives more accurate prediction of the purge flow behavior compared with those early models in literature. In the following sections, we will define the cost function and target range for purge interval, present the model, and investigate the influences of purge interval and cycle duration on the cathode carbon corrosion, power output, hydrogen loss, and lifetime efficiency of a DEA cell.

2. Objective for optimization (cost function)

The objective of this work is to find the purge interval and cycle duration that maximize the efficiency η for a given power level. The DEA cell efficiency, which considers the hydrogen loss during the purge but excludes the BOP components, can be described by:

$$\eta = \frac{\int_0^{t_{tot}} E_{cell} i A dt}{\sum_1^m \Delta h_f \left(Q_{rxt}^{H_2} + Q_{loss}^{H_2}\right)} \quad (1)$$

where Δh_f is the enthalpy of formation of hydrogen fuel in J/mol. The cell is operated under a galvanostatic condition so that the current is constant. The cell voltage E_{cell} is decreasing with time as shown in Fig. 2, therefore integration over a cycle is needed to evaluate the total energy output. The voltage drop within a cycle is reversible, which can be recovered by a purge. The irreversible voltage decay due to carbon corrosion is also captured since the total operating time, t_{tot}, represents multiple cycles (Sec. 4.1). Specifically, t_{tot} equals to $m\Delta t$, where m is the number of DEA cycles. By using different m values, one can either evaluate the efficiency from a single cycle and the subsequent purge (Sec. 5.3), or multiple cycles to reflect the influence of cell degradation (Sec. 5.4). The efficiency η is therefore defined on the lifetime of a DEA cell.

2.1. *Effects of cycle duration and purge interval on efficiency*

The DEA cell efficiency is adversely affected by the amount of hydrogen fuel expelled during the purge. The hydrogen loss during the purge depends on many factors, including the anode pressure, temperature, purge interval and the condition of channel flooding and nitrogen blanketing.

The hydrogen loss in mol at every purge event is calculated by:

$$Q_{loss}^{H_2} = \int_{t_{bp}^j}^{t_{ap}^j} \frac{W_{total}(t,L) n_{H_2}(t,L) P_{AN}}{RT} dt \quad (2)$$

where n_{H_2} is the hydrogen molar fraction at the end of anode channel ($y = L$). The functional dependence of W_{total} ($y = L$) on time is implicit, since W_{total} is expressed as a function of gas composition at the channel end as shown in Eq. (7).

The purge interval can be controlled to achieve $Q_{loss}^{H_2} = 0$, that is, the purge only releases accumulated water and nitrogen at the channel end and it stops when or before the hydrogen front (y_{H_2} in Fig. 3) reaches the channel end. However this purge schedule may not give the best overall efficiency due to remaining trapped nitrogen and water in the anode channel. The optimization methodology developed in this paper can elucidate which purge interval and cycle duration will give the best efficiency.

The 1st term in the denominator in Eq. (1) represents the total hydrogen consumed during a cycle in mol and is calculated from the current density setpoint:

$$Q_{rxt}^{H_2} = \frac{iA}{2F}\Delta t \quad (3)$$

where i is the current density in A cm^{-2}, A is the effective MEA area, and F is the Faraday constant. If the hydrogen loss is not considered, i.e., $Q_{loss}^{H_2} = 0$, Eq. (1) represents the thermodynamic efficiency, that is, the efficiency of the fuel cell electrochemical conversion.

The efficiency defined in Eq. (1) depends on the current setpoint, or the power output in a DEA cycle, which is defined by:

$$P_{DEA} = \frac{1}{\Delta t} \int_{t_{ap}^j}^{t_{bp}^{j+1}} E_{cell} i A dt \quad (4)$$

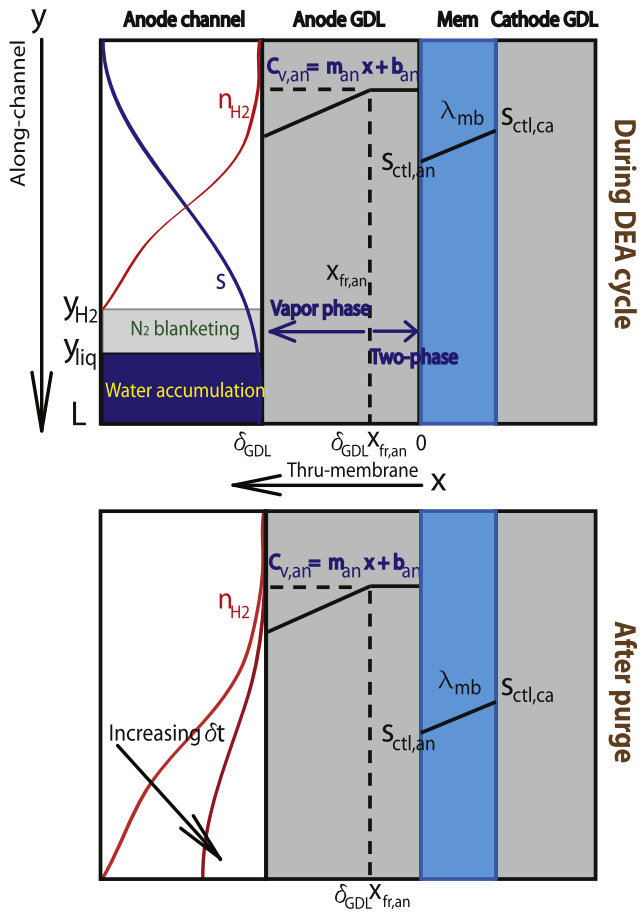

Fig. 3 – A schematic illustrating the modeling domain (not to scale). Species molar fraction (n_i), liquid volume fraction in the channel (s), liquid front in the GDL ($x_{fr,an}$, $x_{fr,ca}$), membrane water content (λ_{mb}) and liquid saturation in the catalyst layer ($s_{ctl,an}$, $s_{ctl,ca}$) are the distributed states along the channel. The liquid water fully occupies the channel when the volume fraction reaches unity. Nitrogen blanketing also contributes to the hydrogen starvation in the channel end. A purge can release the accumulated water and nitrogen, thus restoring the hydrogen concentration in the channel. Increasing purge interval leads to higher average hydrogen concentration right after the purge.

where the right-hand-side integral represents the total energy output in a DEA cycle. Due to the carbon corrosion and associated voltage degradation, the power/energy output in a cycle decreases with time. The power output P_{DEA} is defined on the initial cycle when the system reaches periodic equilibrium. Other operating conditions such as cathode pressure, relative humidity and stoichiometry ratio can also affect the power output by changing the voltage evolution over time.

2.2. *Target range for purge interval*

In DEA operation, a stratified channel distribution with water and nitrogen in the end is expected for a vertically oriented (inlet at the top) cell. As shown in the upper graph of Fig. 3, there is accumulated nitrogen and water in the channel end right before the purge, which leads to local (end of channel) hydrogen starvation and voltage decay. The minimum purge interval, δt_1, places the hydrogen starvation front (y_{H_2}) right at the channel end, i.e., hydrogen becomes available in the whole channel after the purge without any hydrogen loss during the purge. As illustrated in the lower graph of Fig. 3, with an increasing purge interval the hydrogen concentration in the channel becomes higher after the purge, and the power output in the subsequent cycle would be larger, although there is some hydrogen loss during the purge. Finally, the maximum purge interval, δt_2, should fully restore the hydrogen in the channel, i.e., the hydrogen molar fraction (n_{H_2}) exactly reaches unity in the whole channel, leading to the highest power output in the subsequent cycle. These minimum and maximum purge intervals (δt_1 and δt_2) constitute the target range for a purge.

The purge is performed by a solenoid valve at the downstream of the anode outlet. There is physical opening/closing time for the solenoid valve; hence δt_1 needs to be further constrained by a minimum operating time constant t_{SV} of the solenoid valve. In practice, this physical opening/closing time is between 0.01 and 0.5 s. A small value 0.02 s is chosen for t_{SV} in this paper to illustrate the optimization results. The practical target range for purge interval becomes [max(t_{SV}, δt_1), max(t_{SV}, δt_2)].

It is necessary to demonstrate the significance of target range for purge interval. Fig. 4 shows the efficiency as a function of purge interval spanning from 20 ms (t_{SV}) to 900 ms for two selected cycle durations. In the enlarged view, the efficiencies within the target range are presented. It can be seen that the efficiency exhibits very small variation within the target range, as well as a non-monotonic change with increasing purge interval. The efficiency reaches maxima

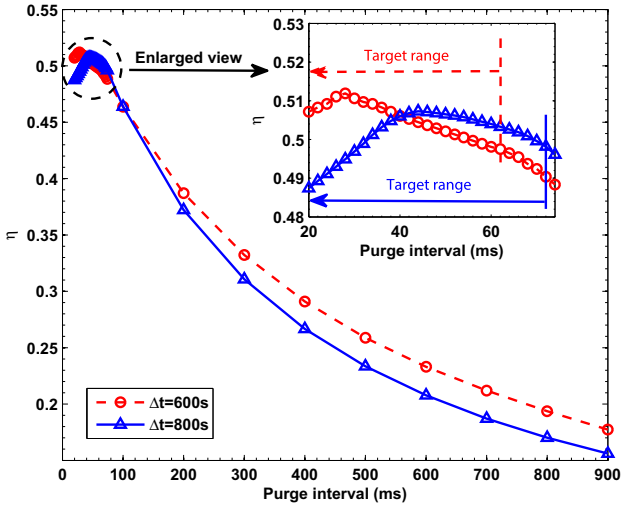

Fig. 4 – The lifetime efficiency with different purge intervals at two selected cycle durations. The definition of lifetime is discussed in Section 4. The operating conditions are: current density 0.6 A/cm^2, cell temperature 50 °C, cathode stoichiometry ratio 3, and *RH* 100%. Monotonic and rapid drop of efficiency has been observed as the purge interval increases beyond the target range.

within the target range but drops rapidly as the purge interval increases beyond the target range. Therefore, identifying the target range is an important step for optimizing efficiency.

3. Model presentation

In previous work [6,8], we have developed a 1-D (along-channel), single-phase transient model to study the nitrogen front evolution and associated carbon corrosion in DEA operation. The model predicted spatio-temporal evolutions of species concentration and carbon corrosion rate have been tuned using the gas chromatography [6] and electrode thickness measurement [27]. The physics based model can also predict the cell equilibrium observed during DEA operation [28]. In this paper we extend our model to capture the liquid water accumulation in the channel end. A model of the channel liquid water is needed because the water impedes the flow of gases during the purge, and a longer purge interval is required to clear the channel when liquid is present.

The model inputs are the nominal current I, cathode inlet relative humidity (RH), and cathode stoichiometry ratio (SR). The cell temperature T and Anode (AN)/Cathode (CA) inlet pressures P_{ca}/P_{an}, are fixed parameters in the model but may be adjusted prior to simulation for different experimental conditions. The model outputs are cell voltage, local current density, molar fraction of each species in the anode, membrane water content, anode/cathode liquid saturation in the catalyst layer, liquid water volume fraction in the anode channel, and liquid front location in the anode/cathode GDL. The cell voltage is a scalar quantity while the other outputs represent the vector of distributed values along the channel (y direction). Fig. 3 illustrates the modeling domain; the two-phase flow in the cathode channel is not modeled for simplicity. Since the model is developed based on our published works [6,29,8], those equations from prior model framework are summarized in Tables 1 and 2 with references.

The initial model assumptions can be summarized as: (1) the model is isothermal; (2) 1+1D (along-channel + through-membrane); (3) the cell degradation is solely due to carbon corrosion in the cathode. More detailed assumptions on each subsystem are discussed in associated subsections.

In Eq. (12) in Table 1, the volume fraction term, $1-s$, is introduced to account for the change of mass due to the volume change from liquid accumulation. When $s = 0$, this equation reduces to the single phase equation of material balance. A similar approach to handle the water phase change in the transport equation can be found in Refs. [30,31]. Only three of the four gas components are independent in this modeling framework. We chose to model the mole fractions of nitrogen (n_{N_2}), oxygen (n_{O_2}) and water vapor (n_V) as our dynamic states. The anode pressure, P_{an}, is assumed to be constant since it is set by an upstream pressure regulator during the DEA operation.

The impact of carbon corrosion on the exchange current density in the Butler–Volmer equation is captured by the effective factor, ϵ_C in Eq. (3), which models the catalytic site loss. The power factor q is a tuned parameter in Ref. [8]. Incorporating ϵ_C in carbon corrosion kinetics leads to an asymptotic drop of corrosion current with constant potential. A more complicated model of Pt loss (such as dissolution and mitigation [32,33]) has not been included in this work, and the carbon corrosion is considered as the sole degradation source.

3.1. Liquid water transport in the anode channel

In literature, there are two common ways to track the two-phase water transport in the channel and GDL: the multi-phase mixture (M^2) [34] and two-fluid models [31]. In this paper, the two-fluid approach is used to track the liquid volume fraction along the channel. Rather than calculating the gas phase velocity from the momentum equation, the total gas flux N_t can be readily converted to velocity, then an interfacial drag coefficient $f(s)$ between liquid and gas phase velocities is used to obtain the liquid phase velocity [31].

Table 1 – Summary of modeling equations.

State/variable	Governing equation		Reference
n_i	$\frac{P_{an}}{RT}\frac{\partial(1-s)n_i}{\partial t} = -\frac{\partial}{\partial y}(J_i + n_i N_t) + r_i \quad \text{for } i \in [N_2, O_2, \text{Vapor}]$	(12)	[6,8]
s	$\rho_w \frac{\partial s}{\partial t} = \rho_w D_s \frac{\partial^2 s}{\partial y^2} - \rho_w \frac{RT}{P_{AN}} \frac{\partial[f(s)N_t(y)]}{\partial y} + M_w\left(r_{V,cond} + \frac{N_{l,an}(x=\delta_{GDL})}{d_{ch}}\right)$	(13)	
λ_{mb}	$\frac{\partial \lambda_{mb}}{\partial t} = \frac{EW}{\rho_{mb}\delta_{mb}}(N_{w,ca,mb} - N_{w,an,mb})$	(14)	[29]
x_{fr}	$\frac{\partial x_{fr,an}}{\partial t} = K_L N_{l,an}$	(15)	[29]
m_C	$\frac{\partial m_C(y,t)}{\partial t} = -\frac{M_C i_{C,CA}}{4F}$	(16)	[8]
$s_{ctl,an}$	$\lambda_{an} = (1 - s_{ctl,an})\lambda^* + s_{ctl,an}\lambda_{max}$	(17)	[29]
E_{cell}, φ_{AN}	$i_{AN} + i_{CA} = 0, \;\; i_{fc} = \frac{1}{L}\int_0^L i_{AN} dy$	(18)	[8]

Table 2 – Physical, transport and kinetic properties.

Quantity	Value	Ref.
Diffusive flux	$J_i = -\frac{P_{AN}}{RT\psi(n)} W \frac{dn_i}{dy}$ (19)	[37]
Convective flux	$N_t(y) = N_t(L) - \int_y^L \left[r_{H_2,rct}(\tilde{y}) + r_{H_2,crs}(\tilde{y}) + r_{N_2,crs}(\tilde{y}) + r_{V,crs}(\tilde{y}) + r_{V,rct}(\tilde{y}) + r_{V,cond}(\tilde{y}) + r_{O_2,crs}(\tilde{y}) + r_{O_2,rct}(\tilde{y}) + \frac{P_{AN}}{RT}\frac{\partial s}{\partial t} \right] d(\tilde{y})$ (20)	[8]
Water condensation source term	$r_{V,cond} = \max\left[0, K_{cond}\frac{(n_V P_{AN} - P_{sat})(1-s)}{RT}\right]$ (21)	
Metal potential at cathode	$V_m^{CA} = V_m^{AN} + E_{cell} + R_{GDL} i_{AN}$ (22)	[8]
Membrane potential at cathode	$\phi_{CA} = \phi_{AN} - R_{mem} i_{AN}$ (23)	[8]
Cathode carbon corrosion	$i_{C,CA} = (1 - s_{ctl,ca})\epsilon_C \gamma_C i_{0,C} L_C \frac{P_{V,CA}}{P^*_{V,CA}} \exp\left[\frac{\alpha_{a,C} F}{RT}\left(V_m^{CA} - \phi_{CA} - V_C^{eq}\right)\right]$ (24)	[8]
Effective factor	$\epsilon_C(y,t) = \left[\frac{m_C(y,t)}{m_{C,0}}\right]^q$ (25)	[38]

Taking into account diffusion, convection and source term, the liquid water volume fraction along the channel is described by the following PDE:

$$\rho_w \frac{\partial s}{\partial t} = \rho_w D_s \frac{\partial^2 s}{\partial y^2} - \rho_w \frac{RT}{P_{AN}} \frac{\partial [f(s) N_t(y)]}{\partial y} + M_w \left(r_{V,cond} + \frac{N_{l,an}(x = \delta_{GDL})}{d_{ch}} \right) \quad (5)$$

where ρ_w is the density of water in kg/m^3, M_w is the molar mass of water in kg/mol, and D_s is the liquid diffusivity in the channel in m^2/s. There are two contributions to the source term in Eq. (5): the first is local vapor condensation ($r_{V,cond}$) in the channel and the other is liquid water flux from the GDL to the channel. The latter, $N_{l,an}$, is zero when the GDL liquid front stays inside the GDL, i.e., not at the GDL/channel interface. Details of the GDL model can be found in Ref. [29].

The convective term $\rho_w(RT/P_{AN})(\partial[f(s)N_t(y)]/\partial y)$ drives the liquid water toward the channel end. As the liquid droplets are carried by gas flow, the corresponding interfacial drag coefficient $f(s)$ is assumed to be a linear function of liquid water volume fraction [31]:

$$f(s) = K_{slip} s \quad (6)$$

where K_{slip} is the physical velocity slip ratio between liquid and gas, which is a tunable parameter in the model. Eq. (6) completes the liquid PDE formulation, Eq. (5).

Due to the high stoichiometry ratio at the cathode, most of the liquid water could be removed by the air flow. Therefore the effect of cathode channel liquid is not included in the model for simplicity.

3.2. *Purge flow*

The exact amount of gas leaving the channel at the purge event is critical to determine the fuel efficiency and voltage recovery. The volumetric flow rate at the outlet is described by [35]:

$$W_{total} = A_o \left(C_{turb} \left[\frac{2}{\rho} \Delta p + \left(\frac{\nu R_t}{2 C_{turb} D_h} \right)^2 \right]^{0.5} - \nu \frac{R_t}{2 D_h} \right) \quad (7)$$

where $C_{turb} = 0.61$ is the dimensionless discharge coefficient under turbulence condition, D_h is the hydraulic diameter of the orifice, A_o is the area of the orifice (solenoid valve port), $R_t = 9.33$ is the critical purge parameter from Ref. [35]. Also, ρ is the density of the mixture flow (liquid water and multiple gas species); ν, defined as μ/ρ, is the kinematic viscosity of the mixture flow, and Δp is the differential pressure across the orifice. Since the local species molar fraction varies with the channel length and thus purge time, integrating W over the purge interval gives the volumetric displacement of accumulated gas at the channel end. The total outlet flow is assumed to be evenly distributed between the parallel channels, therefore $W_{chan} = W_{total}/k$ where k is the number of parallel channels in the anode. The factor $1/k$ scales the total outlet flow for simulations are performed on a single channel.

Since the purge interval is very short (in a scale of ms), the profiles of molar fractions (n_i) and flow rate (W_{chan}) at the end of a DEA cycle are assumed to move along the channel direction during the purge without the diffusion effects, which is a typical plug flow behavior.

The density ρ and viscosity ν at the outlet are dependent on the gas composition and liquid volume fraction. The density ρ can be defined by:

$$\rho(y) = (1 - s)\rho_g + s\rho_w \quad (8)$$

$$\rho_g(y) = \rho_{N_2} n_{N_2} + \rho_V n_V + \rho_{O_2} n_{O_2} + \rho_{H_2}(1 - n_{N_2} - n_V - n_{O_2}) \quad (9)$$

in which ρ_w is the density of liquid water, and ρ_g is the density of gas mixture. The viscosity is defined similarly. Since the local gas composition varies along the channel, the density/viscosity of the gas mixture is a function of y.

4. Model validation and simulation results

The above DEA oriented two-phase fuel cell model is tuned and validated with the experimental data. The details of the experiment are described in a prior publication [3]. The parameters relevant to the gas species distribution along the channel have been tuned against the GC sample data in our prior work [8]. Table 3 summarizes the parameter values used in the along-channel model. There are two steps in implementing the model: the coupled multi-state PDE system representing the DEA cycle is solved first, followed by the purge flow submodel which calculates the hydrogen loss and redistributes all states as the initial condition of the subsequent DEA cycle. This two-step implementation repeats for 100–1200 times depending on the cycle duration to simulate the cell lifetime. Finally, the efficiency is evaluated after finishing the simulation and collecting the data. The coupled PDE system is solved using a variable step solver, Matlab ODE15s, with a relative tolerance of $1e^{-4}$. The channel is discretized using a 2nd order approximation of the spatial derivatives on a 51-point grid.

Table 3 – Geometrical, physical and operating parameters.

Quantity	Value
Catalyst loading L_{Pt}	3×10^{-4} g cm^{-2}
Electrochemical area of Pt γ_{Pt}	6×10^{5} cm^2 g^{-1}
Electrochemical area of carbon γ_C	6×10^{6} cm^2 g^{-1}
Anodic transfer coefficient for carbon corrosion $\alpha_{a,C}$	0.25
Exchange current density of carbon corrosion $i_{0,C}$	2.5×10^{-10} A cm^{-2}
Equilibrium potential for carbon corrosion V_C^{eq}	0.21 V
Anode metal potential V_m^{AN}	0 V
Initial carbon loading per unit MEA area $m_{C,0}$	0.002 g cm^{-2}
Cathode reference pressure $P^*_{i,CA}$, i = [O_2, vapor]	1.2355×10^5 Pa
Anode inlet pressure P_{AN}	4.0 psig
Cathode system pressure P_{CA}	3.6 psig
Cell temperature T	323 K
Hydrogen enthalpy of formation Δh_f	-242×10^3 J/mol
Discharge coefficient C_{turb}	0.61
Critical value for purge flow model R_t	9.33
Area of purge orifice A_o	0.37 mm^2
Hydraulic diameter of purge orifice D_h	1.9 mm
Tunable power factor for remaining carbon, q	1.5
Effective MEA area A	50 cm^2
Number of anode channels k	25
Anode/Cathode channel depth $h_{ch,an/ca}$	0.18/0.10 cm
Channel width w_{ch}	0.07 cm^2
Channel length l	7.27 cm^2
Membrane thickness δ_{mb}	25 μm
GDL thickness δ_{GDL}	300 μm
Density of hydrogen ρ_{H_2}	0.0899 kg/m^3
Density of nitrogen ρ_{N_2}	1.25 kg/m^3
Density of vapor/liquid water ρ_V/ρ_w	0.0829/997 kg/m^3
Viscosity of hydrogen ν_{H_2}	100.1×10^{-6} m^2/s
Viscosity of nitrogen ν_{N_2}	14.2×10^{-6} m^2/s
Viscosity of vapor/liquid water ν_V/ν_w	$144.8/0.553 \times 10^{-6}$ m^2/s
Water transfer coefficient γ_w	5.7×10^{-6} m/s
Molar mass of water M_w	0.018 kg/mol
Condensation rate constant K_{cond}	1000 l/s
Mass transport coefficient γ	0.1 m/s
Liquid water diffusivity D_s	1 m^2/s
Vapor diffusivity in anode GDL D_v	1.25×10^{-4} m^2/s
Slip ratio between liquid and gas K_{slip}	0.6
Number of channel meshes in numerical computation N	51

The data set with high current load (0.6 A/cm^2) and high cathode *RH* (100%), which leads to sufficient liquid water accumulation in the anode, is selected for simulation. Fig. 5 compares the tuned model and experiment. The cell used in the experiment comprised of a Nafion 111-IP membrane (25.4 μm thick) with Pt loading of 0.3 mg cm^{-2} at both sides, and two SGL 10BB nonwoven carbon papers at both sides with uncompressed thickness of 420 μm and porosity of 0.84. The catalyst coated membrane (CCM) was purchased from Ion Power, Inc., however the information of the support carbon type and loading was not released by the company. The purge was triggered as the cell voltage reduced to 0.4 V in the experiment, hence the cycle duration varies from ~700 s to ~900 s. The cell voltage experienced an abrupt drop as the cathode stoichiometry ratio was reduced from 3 to 2.

The model predicted voltage evolution agrees with the experimental data. The liquid effects are captured by $s_{ctl,an}$, $s_{ctl,ca}$ and s. The predicted increasing liquid mass within a cycle is consistent with the experimental data, as shown in the third subplot of Fig. 5. The liquid mass from the experiment did not drop at the end of the second cycle, probably due to the droplet plugging in the cell manifold.

Other simulation results are summarized in Fig. 6. The simulation starts with a fully humidified membrane ($\lambda_{mb} = 12$) to account for the operation history of the cell. It can be seen that the membrane water content remains at a high level during the whole period. Liquid saturation in the cathode catalyst layer is substantially higher than the anode in the channel inlet and middle regions, which drives the water transport from cathode to anode. The model predicts hydrogen starvation at the 0.9 fractional channel location at $t = \sim 770$ s. Finally, the seventh subplot indicates that the liquid front stays at the GDL/channel interface only at the channel end region. In other regions of the channel, liquid water comes from local condensation.

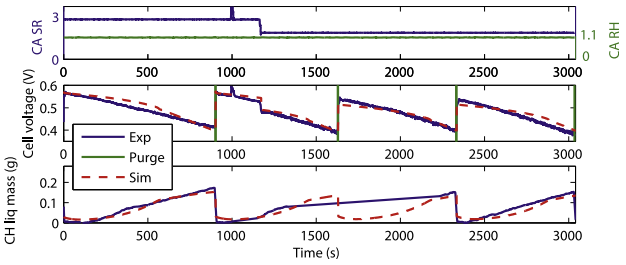

Fig. 5 – Comparison between tuned model and experiments at current density 0.6 A/cm^2, cell temperature 50 °C, anode/cathode pressure 4.0/3.6 psig, cathode stoichiometry ratio 3 and 2, and *RH* 100%.

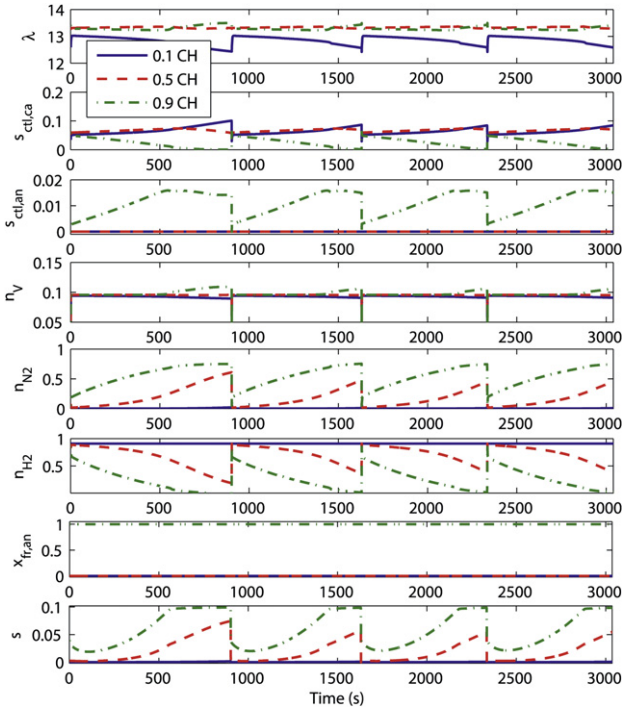

Fig. 6 – Simulation results from the same operating conditions as in Fig. 5 (cathode stoichiometry ratio is 3 except stated otherwise). Each subplot shows the evolutions of a specific parameter at the inlet, middle and end regions of the channel. These subplots present the simulation results of membrane water contents, liquid saturation in the cathode and anode catalyst layers, molar fractions of vapor, nitrogen and hydrogen, dimensionless liquid front in the anode GDL, and channel liquid volume fraction, respectively.

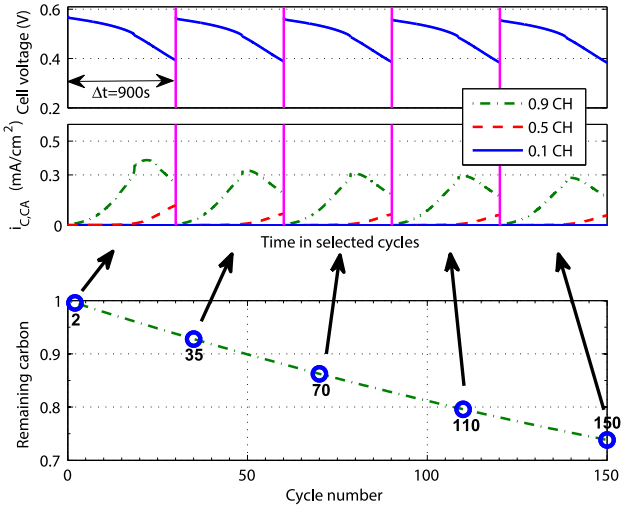

Fig. 7 – Simulation results of 150 continuous DEA cycles. The results from selected DEA cycles, rather than the entire data set, are examined in details as indicated by the arrows. The vertical pink lines represent the purge events. The cycle duration is 900 s and the purge interval is 54 ms. The operating conditions are consistent with the validated case in Fig. 5: current density 0.6 A/cm^2, cell temperature 50 °C, cathode stoichiometry ratio 3, and *RH* 100%. The first subplot shows the cell voltage. The second subplot illustrates the cathode carbon corrosion current in the inlet, middle and end regions of the channel. The third subplot presents the percentage remaining carbon in the cathode catalyst layer at 0.9 fractional channel location throughout the whole lifetime. (For interpretation of the references to color in this figure legend, the reader is referred to the web version of this article.)

4.1. *Predicting carbon corrosion and cell lifetime*

The target of a fuel cell lifetime is ~5000 h in automotive applications to compete with the conventional powertrain, and voltage degradation rate of 2–10 μV h^{-1} is generally acceptable with flow-through operations [36]. In this paper, therefore, we define the occurrence of a 10 mV irreversible voltage drop in DEA operation as the end of "life". The model can be used to predict the cell lifetime under continuous DEA cycling. The carbon loss is captured by Eq. (16), which affects the carbon corrosion rate and terminal voltage over time by Eq. (24).

Fig. 7 presents the lifetime simulation results, i.e., the remaining carbon at the channel end region within 150 continuous DEA cycles, and the voltage and corrosion current evolutions in selected cycles. The cycle duration is 900 s and the purge interval is 54 ms. The time-evolution of the terminal voltage and carbon corrosion current at three representative locations along the channel (inlet, middle and outlet) for the 5 selected DEA cycles are shown in the upper subplots of Fig. 7. The operating conditions are the same as the validated case in Fig. 5. The cell voltage at the 150th cycle exhibits ~10 mV irreversible voltage loss compared with the initial cycle, corresponding to ~25% carbon loss in the cathode catalyst layer at 0.9 fractional channel location near the end of the channel and ~11% overall carbon loss in the whole channel. The remaining carbon at the channel end is illustrated by the second subplot; the cathode carbon corrosion rate at the channel end is substantially higher than in other regions due to the local fuel starvation.

5. Optimization of purge schedule

The target range for the purge interval depends on the gas and liquid water distribution in the anode channel at the end of the cycle. Fig. 8 shows a simulation used to determine the target range for the purge interval. At the end of a DEA cycle or the start of a purge ($t = t_{bp}$), liquid water accumulates in the channel end, where complete hydrogen starvation with zero molar fraction is also observed.

5.1. *Determining the target range for purge interval*

The minimum purge time, δt_1, is designed to release the accumulated water/nitrogen and to place the hydrogen

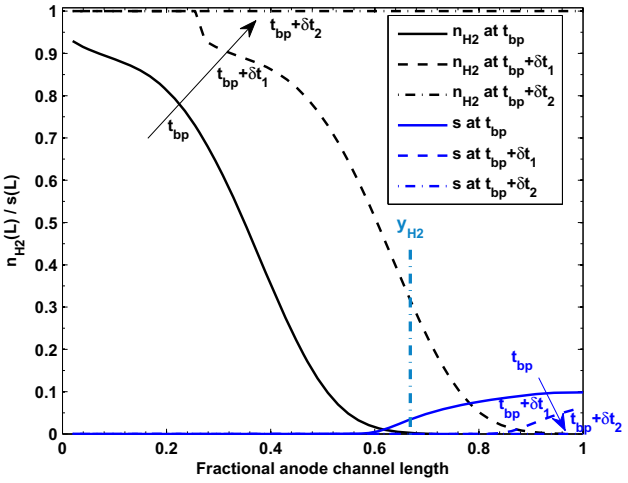

Fig. 8 – Distribution of hydrogen concentration and liquid volume fraction before and after purge at operating conditions of cycle duration 1100 s, current density 0.6 A/cm^2, cell temperature 50 °C, cathode *RH* 0.9, stoichiometry ratio 3 and pressure 1.18 bar. The black curves show the hydrogen molar fraction and the blue ones show the liquid volume fraction in the anode channel. The hydrogen starvation front y_{H_2} before the purge is also shown. Minimum purge interval should be chosen to place the hydrogen starvation front at the channel end, and maximum one exactly and fully restore the hydrogen in the channel without further loss. (For interpretation of the references to color in this figure legend, the reader is referred to the web version of this article.)

starvation front at the channel end. Due to the high purge flow rate (diffusion can be ignored), the profile at $t = t_{bp} + \delta t_1$ consists of a shift of the hydrogen profile at $t = t_{bp}$ toward the channel end plus a hydrogen restored region ($n_{H_2} = 1$) in the channel inlet. In other words, the purge flow behaves as plug flow. With the minimum purge interval δt_1, there is no hydrogen loss during the purge; however the hydrogen concentration is low in the channel, which would adversely affect the energy output in the subsequent cycle. If the purge is extended to $t = t_{bp} + \delta t_2$ when the hydrogen molar fraction reaches unity in the whole channel, then the energy output in the subsequent cycle would be the highest, although there is some hydrogen loss during the purge.

Mathematically, δt_1 and δt_2 satisfy:

$$L - \int_{t_{bp}}^{t_{bp}+\delta t_1} \frac{W_{total}}{k w_{ch} d_{ch}} dt = y|_{n_{H_2}=0, t=t_0} \quad (10)$$

$$L - \int_{t_{bp}}^{t_{bp}+\delta t_2} \frac{W_{total}}{k w_{ch} d_{ch}} dt = 0 \quad (11)$$

in which W_{total} is the volumetric purge flow rate defined in Eq. (7).

In Fig. 8 the hydrogen starvation occurs before the purge. There exists a special scenario: when the cycle duration is very short, then it is possible that hydrogen starvation does not occur even at the channel end. Under that circumstance, there would inevitably be a certain amount of hydrogen loss during any purge. Therefore the lower limit of the target range for small cycle duration is always t_{SV}. The target range for purge interval in general is dependent on the cycle duration.

5.2. *Influences of cycle duration*

In this subsection we investigate the influence of cycle duration on carbon corrosion and cell efficiency. The purge interval is set to a constant, $\delta t = 20$ ms. The cycle duration affects both the cathode carbon corrosion rate within a cycle and the hydrogen loss during the purge.

The DEA cell efficiency as the objective should also be considered when determining the optimum cycle duration. Fig. 9 shows the channel end hydrogen concentration at the cycle end and the hydrogen loss during the purge as a function of cycle duration with a fixed purge interval. When the cycle duration becomes shorter, there is still hydrogen at the channel end right before the purge, and thus unavoidable hydrogen loss. Wasted hydrogen during the purge reduces the DEA cell efficiency through $Q_{loss}^{H_2}$ term in Eq. (1). The hydrogen loss is substantially reduced as the cycle duration extends beyond 600 s, because hydrogen starvation occurs at the channel end region with extended cycle duration and therefore the purge removes less hydrogen and more nitrogen and liquid water. The thermodynamic efficiency increases with shorter cycle duration as indicated by the terminal voltage as shown in Fig. 10. However $Q_{loss}^{H_2}$ also increases with shorter cycle duration. The efficiency in the third subplot of Fig. 9 shows a non-monotonic evolution against cycle duration. The hydrogen loss is dominant due to the increasing efficiency when the cycle duration is smaller than 600 s.

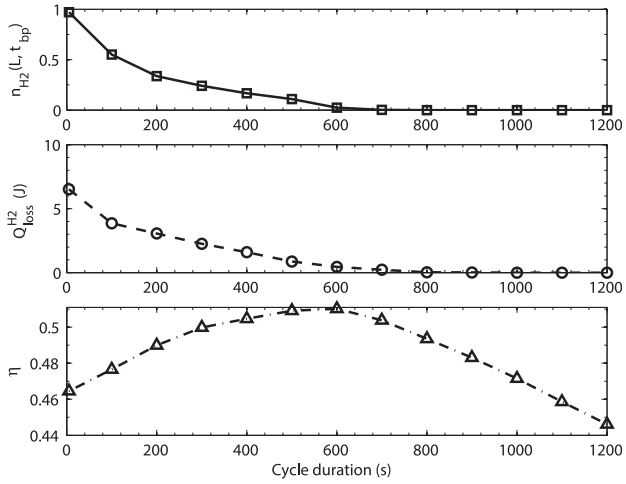

Fig. 9 – Influences of cycle duration. The operating conditions are consistent with the validated case in Fig. 5. The first subplot indicate the influence of increasing cycle duration on the hydrogen molar fraction at the channel end right before the purge. The second subplot shows the hydrogen loss in Joule. The third subplot indicates the efficiencies evaluated over one DEA cycle together with the subsequent purge. The purge interval is fixed at 20 ms.

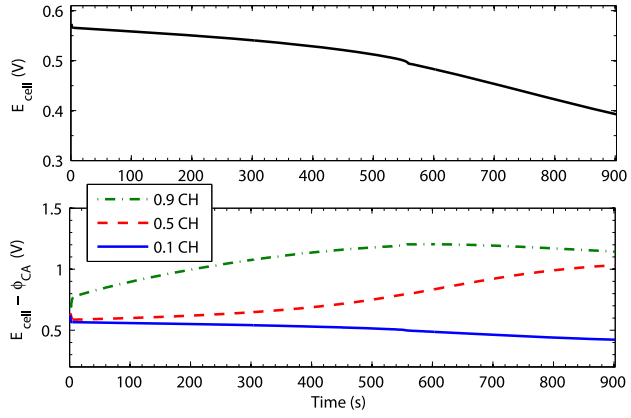

Fig. 10 – Evolution of cathode interfacial potential within a DEA cycle. The operating conditions are consistent with the validated case in Fig. 5. The upper subplot shows the model predicted cell voltage within a 900 s cycle. The lower subplot illustrates the cathode interfacial potential at the inlet, middle and end regions of the channel. At the end region a non-monotonic evolution trend with time has been observed.

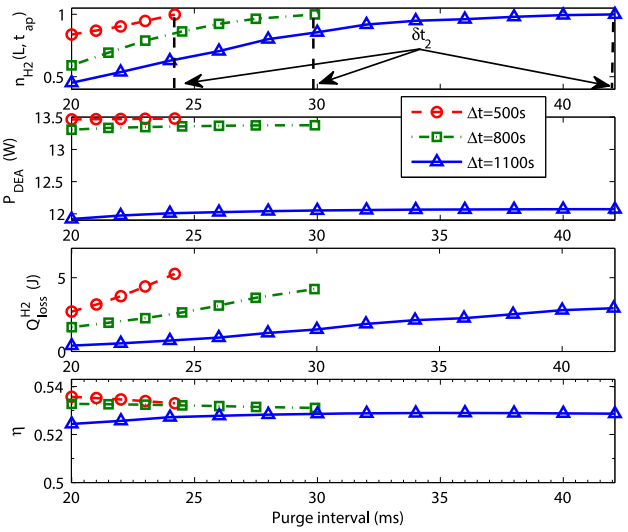

Fig. 11 – The influences of purge interval and cycle duration, with operating conditions being: current density 0.4 A/cm^2, cell temperature 50 °C, cathode *RH* 0.9, stoichiometry ratio 3 and pressure 1.18 bar. The simulation results are collected after the system reaches periodic steady state. The three colored curves with markers represent the simulation results obtained from three different cycle durations. The *x*-limits of each curve indicate δt_{min} and δt_{max} for that cycle duration. The first subplot shows the hydrogen molar fraction at the channel end after the purge. The second subplot presents the power outputs in the subsequent cycle after the purge. The third subplot indicates the hydrogen loss during the purge with different purge intervals. Finally, the fourth subplot shows the efficiencies evaluated over one DEA cycle together with different purge intervals.

Fig. 10 illustrates the evolution of cell voltage and cathode interfacial potential within a DEA cycle. The cycle duration is 900 s and the operating conditions are the same with the validated case in Fig. 5. The cathode interfacial potential, $E_{cell} - \phi_{CA}$, determines the kinetics of cathode carbon corrosion as shown in Eq. (24). It is much higher at the channel end compared with other regions due to the fuel starvation. The cathode interfacial potential at the channel end is therefore the main concern. As shown in the upper subplot, the cell voltage decreases with time due to the hydrogen depletion which effectively reduces the corrosion rate. Meanwhile the membrane phase potential at the channel end becomes more negative, which increases the corrosion rate. If the cycle duration is extended, the carbon corrosion rate at the channel end would decrease after reaching a peak value at ~650 s. That is to say, further postponing a purge after reaching the peak cathode interfacial potential would be beneficial for protecting carbon, although the cell voltage decreases significantly. If there are no other constraints on cycle duration, a shorter cycle is preferred because of the increased energy output and reduced carbon corrosion during DEA cycling.

5.3. *Influences of purge interval*

In this subsection, the influences of purge interval are examined with fixed cycle duration. The model can be used to evaluate the trade-off between hydrogen loss and increased energy output for a single cycle. The objective function thus becomes $\eta = (\int_{t_{ap}^{j}}^{t_{ap}^{j+1}} E_{cell} i A dt)/(\Delta h_f (Q_{rxt}^{H_2} + Q_{loss}^{H_2}))$. The effect of carbon corrosion is not shown because it affects the integral in the numerator only after multiple cycles. Fig. 11 summarizes the simulation results. Three cases with different cycle durations are examined. The target range of purge interval depends on the cycle duration. In Fig. 11, the range of purge interval presented corresponds to the target range of that particular cycle duration (500 s, 800 s and 1100 s).

The hydrogen molar fraction at the channel end increases with purge interval and reaches unity at δt_2 as shown in the first subplot of Fig. 11. The second subplot indicates that an extended purge indeed leads to a larger power output since the hydrogen concentration is higher during the subsequent DEA cycle. On the other hand, it would produce a larger amount of hydrogen loss, as shown in the third subplot. The competing influence of hydrogen loss and increased terminal voltage on the overall efficiency as a function of purge interval is shown in the last subplot of Fig. 11. For the cases with $\Delta t = 500$ and 800 s, increasing purge interval leads to lower cell efficiency. However for longer cycle durations, when hydrogen starvation occurs at the channel end, the slope of the efficiency versus purge interval is non-monotonic. Therefore, the shortest duration does not yield the highest efficiency. In this case a maximum efficiency of 52.9% is reached, after which the efficiency slightly decreases. These findings indicate that if complete hydrogen starvation has not been observed in the channel end, reducing the hydrogen loss is more significant than restoring the hydrogen concentration in the anode. Even with complete hydrogen starvation

($\Delta t = 1100$), $\delta t = 36$ ms, rather than $\delta t_2 = 42.1$ ms, gives the largest efficiency.

The calculated efficiencies do not show substantial differences (<2%), because the purge interval is already constrained in the target range. This suggests that as long as the purge interval lies within the target range, then its influences on the efficiency may be negligible.

5.4. *Optimization of cycle duration and purge interval over cell lifetime*

In prior subsections we examined the influences of cycle duration on carbon corrosion and purge interval on DEA cell efficiency. In general, shorter cycle duration and longer purge interval are beneficial for achieving higher thermodynamic efficiency and protecting support carbon in the cathode; however, the hydrogen loss would be higher under these conditions. The subject of this optimization study is to investigate the trade-off between wasted hydrogen and reducing the corrosion rate over a longer time horizon. The efficiency of a DEA cell, calculated using Eq. (1), is evaluated over the whole lifetime. In this work the cell lifetime is defined by the occurrence of 10 mV irreversible voltage drop. Since the cycle duration and purge interval both affect the lifetime, we use the shortest lifetime among all cases as the simulation time interval for comparing the efficiencies. In this subsection we consider cycle duration and purge interval simultaneously as the variables and search for the maximum (optimum) lifetime efficiency, Eq. (1), within a 2-D space by simulating the efficiency over the cell lifetime. The operating conditions are the same with the validated case: current density 0.6 A/cm^2, cell temperature 50 °C, cathode *RH* 100% and stoichiometry ratio 3, and anode/cathode pressure 4.0/3.6 psig.

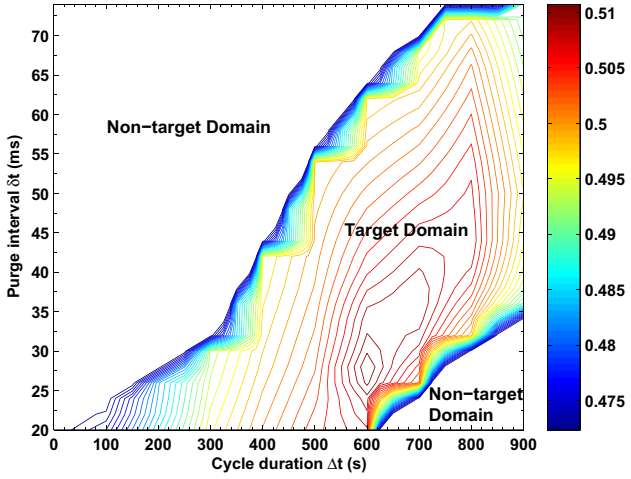

Fig. 12 – The contour plot showing the target domain and the lifetime efficiencies therein given fixed amount of operating time. The last subplots in Figs. 9 and 11 can be considered as the vertical and horizontal slices from the contour map, although only one cycle is evaluated as opposed to lifetime. The contour map shows that the maximum efficiency is achieved with cycle duration of 600 s and purge interval of 28 ms.

Fig. 12 illustrates the 2-D target domain in which the optima lies, as well as the calculated efficiencies within the domain. The target range for purge interval is calculated after the system reaches periodic steady state. The calculated target range for each purge interval, [max(t_{SV}, δt_{min}), max(t_{SV}, δt_{max})], is reflected by the vertical limits of the domain. The target range for cycle duration is defined as follows: its lower limit can go as small as zero, in which case it becomes a flow-through operation. Its upper limit is defined as the amount of time to reduce the cell voltage to 0.4 V. In Fig. 12, these two limits are 0 and 900 s, respectively. When the cycle duration is extremely short ($\Delta t = 50$ s and zero), the target range for purge interval shrinks to a single point, t_{SV}, because the very high hydrogen concentration in the channel leads to a large purge flow rate. When the cycle duration is less than 600 s, t_{SV} is always the lower limit of the target range.

Since the efficiency (Eq. (1)) depends on the two design variables, Δt and δt, the search of optima is performed by scanning the target domain with coarse grids first. A further scan with finer grids would be performed if necessary until the optima can be located with satisfactory accuracy. The two-step scheme in scanning the domain can reduce the computational expense. In Fig. 12, the grid distance for purge interval is 2 ms and for cycle duration 100 s.

At each grid represented by a combination of Δt and δt, the efficiency is collected to generate the contour plot. Because the cell durability is concerned, the total DEA operating time should be identical when evaluating the efficiency at each grid. The operating time is determined from the cell lifetime using the operating schedule that gives the worst durability, namely, longest cycle duration with shortest purge interval. In Fig. 12, they are 900 s and 34.1 ms, respectively. For this operating schedule, after 132 DEA cycles the cell voltage observes 10 mV irreversible drop, and the cell lifetime is reached according to the prior definition. The total operating time is thus 132×900 s = 33 h. The necessary DEA cycle numbers for other operating schedules are then calculated to satisfy an identical operating time. For shorter cycle durations or longer purge intervals, the actual voltage degradations at the end of 33 h are smaller than 10 mV as shown in Fig. 13, which also plots the energy outputs throughout the total operating time for different cycle durations. Shorter cycle duration leads to higher energy or power output, and smaller voltage degradation, although the efficiency may be low with a short cycle duration. The difference in energy output is enlarged by the more severe cell degradation at longer cycle duration.

The optimum efficiency is ~50.9%, as shown in the contour plot in Fig. 12. The variation of efficiency within the target domain is less than 4%. Motivated by this finding, we conducted a parametric study of current setpoint on the target domain as shown in Fig. 14. At reduced current setpoint (power level), it takes a longer time to reduce the voltage to 0.4 V and there is a smaller amount of liquid water at the end of a cycle. As a result, with decreasing current density the target range for cycle duration becomes larger, whereas that for purge interval becomes smaller. One can simply calculate the target domain for the selected power as illustrated in Fig. 14, then use $0.5 \times (\delta t_1 + \delta t_2)$ as the optimized purge interval. The maximum achievable efficiency shown in Fig. 14, which increases with decreasing current loads, can be used as

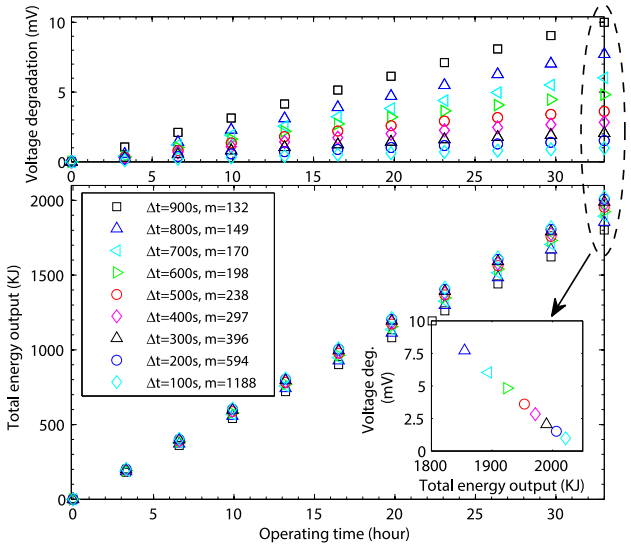

Fig. 13 – Voltage degradation and total energy output in 33 h DEA operation for different cycle durations with minimum purge intervals in the target domain. The cycle duration (Δt) and the corresponding number of cycles (*m*) are noted in the legend. With the same simulation time, the enlarged view shows the voltage degradation versus total energy output at the end of 33 h for nine different cycle durations.

a criterion for choosing an operating condition, since the efficiency variation within the target domain is small.

In Fig. 12, increasing cycle duration beyond 800 s or decreasing cycle duration within 500 s decreases the efficiency. With a medium cycle duration (Δt = 600 s) the achievable efficiency is highest. For purge interval, if the cycle

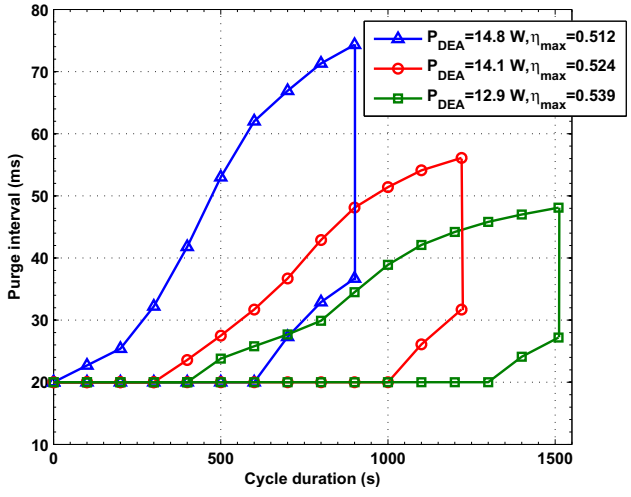

Fig. 14 – The target domains with different current setpoints (0.6, 0.5 and 0.4 A/cm^2) or power levels (14.8, 14.1 and 12.9 W). Other operating conditions (cell temperature 50 °C, cathode *RH* 100% and stoichiometry ratio 3, and anode/cathode pressure 4.0/3.6 psig) are the same for three cases. The power in the legend is the average one calculated from P_{DEA} for all cycle durations and purge intervals within the target domain.

duration is longer than 800 s, the efficiency reaches maximum at medium δt, whereas it decreases as it approaches δt_1 and δt_2. Complete hydrogen starvation due to water accumulation and nitrogen blanketing, which is associated with longer cycle durations, greatly accelerates the carbon corrosion in the channel end region. When the cycle duration is very long ($\Delta t > 800$ s), a medium purge interval, rather than complete purge, leads to the maximum efficiency. The efficiency still decreases beyond the maximum value with increasing purge intervals, which suggests that hydrogen loss is more influential than carbon corrosion under such conditions. When $\Delta t < 500$ s, the efficiency decreases monotonically with increasing purge intervals and the minimum purge interval is preferred, because hydrogen loss becomes the sole concern.

The optimum appears at medium cycle duration. Because large Δt results in severe hydrogen starvation and associated carbon corrosion, whereas small Δt leads to substantial hydrogen in the channel end region before the purge and associated hydrogen loss during the purge. It is essential not to purge the cell too early with substantial hydrogen in the channel end. The DEA operation with small Δt generally exhibits a lower efficiency but produces higher energy output as shown in the lower subplot of Fig. 13.

6. Conclusions

In this paper, we focus on the optimization of the DEA operating schedule determined by purge interval and cycle duration. We extended the along-channel, single-phase and transient DEA model in Ref. [8] to capture the liquid water transport and accumulation in the anode channel end, as well as the purge flow behavior. These improvements were necessary to accurately predict water and nitrogen accumulation in the anode channel and the resulting hydrogen loss during the purge. The target ranges for purge interval are defined based on the channel gas composition at the end of the cycle duration.

We then investigated the influence of cycle duration and purge interval on carbon corrosion and DEA cell efficiency. There exists a trade-off between maximizing the thermodynamic efficiency during the DEA cycle and minimizing hydrogen loss during the purge. Shorter cycle durations and longer purge intervals tend to increase the thermodynamic efficiency; however, longer cycle durations and shorter purge intervals can reduce the amount of hydrogen loss. The optimization is performed by collecting the lifetime simulation data at each grid within the 2D target domain for cycle duration and purge interval. It is found that a medium cycle duration without severe hydrogen starvation at the channel end together with a short purge interval leads to the highest DEA cell efficiency at current density of 0.6 A/cm^2. For long cycle durations, severe hydrogen starvation due to water accumulation and nitrogen blanketing accelerates the carbon corrosion particularly in the channel end region, which requires an increased purge interval, but not a complete purge, to achieve highest efficiency. For short cycle durations, however, the minimum purge interval is preferred, suggesting that reducing hydrogen loss is more important than removing nitrogen and water. The small variation of efficiency (~4%) within the target domain suggests that as long as the purge

interval can be selected from the target range, further optimization may not be necessary. Decreasing the current set-point from 0.6 to 0.4 A/cm^2 changes the target domain, and increases the maximum obtainable efficiency.

The analysis and methodology presented in this paper can be used for the design of a DEA fuel cell system. The optimum purge interval and cycle duration vary with the operating conditions and the physical specifications of solenoid valve. In the future, the optimized purge behavior and associated voltage degradation will be compared to experimental data. Further modeling work is necessary for investigating the effect of other DEA system parameters such as cathode stoichiometry.

Acknowledgments

This work is funded by the National Science Foundation through CBET-0932509 and Ford Motor Company.

REFERENCES

[1] Mocoteguy P, Druart F, Bultel Y, Besse S, Rakotondrainibe A. Monodimensional modeling and experimental study of the dynamic behavior of proton exchange membrane fuel cell stack operating in dead-end mode. Journal of Power Sources 2007;167:349–57.
[2] McKay D, Siegel JB, Ott W, Stefanopoulou AG. Parameterization and prediction of temporal fuel cell voltage behavior during flooding and drying conditions. Journal of Power Sources 2008;178:207–22.
[3] Siegel JB, McKay D, Stefanopoulou AG, Hussey D, Jacobson D. Measurement of liquid water accumulation in a PEMFC with dead-ended anode. Journal of the Electrochemical Society 2008;155:B1168–78.
[4] Ahluwalia RK, Lajunen A, Wang X, Kumar R. Fuel cells systems analysis, DOE hydrogen program review. Washington, DC; May 2012.
[5] Ahluwalia RK, Wang X. Fuel cell systems for transportation: status and trends. Journal of Power Sources 2008;177:167–76.
[6] Siegel JB, Bohac S, Stefanopoulou AG, Yesilyurt S. Nitrogen front evolution in purged polymer electrolyte membrane fuel cell with dead-ended anode. Journal of the Electrochemical Society 2010;157:B1081–93.
[7] Lee Y, Kim B, Kim Y. An experimental study on water transport through the membrane of a PEFC operating in the dead-end mode. International Journal of Hydrogen Energy 2009;34:7768–79.
[8] Chen J, Siegel JB, Matsuura T, Stefanopoulou AG. Carbon corrosion in PEM fuel cell dead-ended anode operations. Journal of the Electrochemical Society 2011;158:B1164–74.
[9] Curtin D, Lousenberg R, Henry T, Tangeman P, Tisack M. Advanced materials for improved PEMFC performance and life. Journal of Power Sources 2004;131:41–8.
[10] Mittal V, Kunz H, Fenton J. Membrane degradation mechanisms in PEMFCs. Journal of the Electrochemical Society 2007;154:B652–6.
[11] Secanell M, Wishart J, Dobson P. Computational design and optimization of fuel cells and fuel cell systems: a review. Journal of Power Sources 2011;196:3690–704.
[12] Grujicic M, Chittajallu K. Optimization of the cathode geometry in polymer electrolyte membrane (PEM) fuel cells. Chemical Engineering Science 2004;59:5883–95.
[13] Lin H-H, Cheng C-H, Soong C-Y, Chen F, Yan W-M. Optimization of key parameters in the proton exchange membrane fuel cell. Journal of Power Sources 2006;162:246–54.
[14] Song D, Wang Q, Liu Z, Navessin T, Eikerling M, Holdcroft S. Numerical optimization study of the catalyst layer of PEM fuel cell cathode. Journal of Power Sources 2004;126:104–11.
[15] Secanell M, Carnes B, Suleman A, Djilali N. Numerical optimization of proton exchange membrane fuel cell cathode electrodes. Electrochimica Acta 2007;52:2668–82.
[16] Wu J, Liu Q, Fang H. Toward the optimization of operating conditions for hydrogen polymer electrolyte fuel cells. Journal of Power Sources 2006;156:388–99.
[17] Wu W, Lin Y-T. Fuzzy-based multi-objective optimization of DMFC system efficiencies. International Journal of Hydrogen Energy 2010;35:9701–8.
[18] Wishart J, Dong Z, Secanell M. Optimization of a PEM fuel cell system based on empirical data and a generalized electrochemical semi-empirical model. Journal of Power Sources 2006;27:1041–55.
[19] Zhao H, Burke AF. Optimization of fuel cell system operating conditions for fuel cell vehicles. Journal of Power Sources 2009;15:408–16.
[20] Hikita S, Nakatani F, Yamane K, Takagi Y. Power-generation characteristics of hydrogen fuel cell with dead-end system. JSAE Review 2002;23:177–82.
[21] Dumercy L, Pera M-C, Glises R, Hissel D, Hamandi S, Badin F, et al. PEFC stack operation in anodic dead end mode. Fuel Cells 2004;4:352–7.
[22] Himanen O, Hottinen T, Tuurala S. Operation of a planar free-breathing PEMFC in a dead-end mode. Electrochemistry Communications 2007;9:891–4.
[23] Choi JW, Hwang Y-S, Cha SW, Kim MS. Experimental study on enhancing the fuel efficiency of an anodic dead-end mode polymer electrolyte membrane fuel cell by oscillating the hydrogen. International Journal of Hydrogen Energy 2010;35:12469–79.
[24] Dehn S, Woehr M, Heinzel A. Development of a near-dead-ended fuel cell stack operation in an automotive drive system. In: Vehicle power and propulsion conference (VPPC), IEEE, 2011.
[25] Yang T, Shi P. A preliminary study of a six-cell stack with dead-end anode and open-slits cathode. International Journal of Hydrogen Energy 2008;33:2795–801.
[26] Mokmeli A, Asghari S. An investigation into the effect of anode purging on the fuel cell performance. International Journal of Hydrogen Energy 2010;35:9276–82.
[27] Matsuura T, Siegel JB, Chen J, Stefanopoulou AG. Multiple degradation phenomena in polymer electrolyte fuel cell operation with dead-ended anode. In: Proceeding of ASME 2011 5th international conference on energy sustainability & 9th fuel cell science, engineering and technology conference. Washington D.C.; 2011.
[28] Chen J, Siegel JB, Stefanopoulou AG. Nitrogen blanketing front equilibria in dead end anode fuel cell operation. In: American control conference. 2011. p. 1524–9.
[29] Siegel JB, Stefanopoulou AG, Ripaccioli G, Di Cairano S. Purge scheduling for dead-ended anode operation of PEM fuel cells. In: The control handbook: control system applications. 2nd ed. CRC Press; 2010.
[30] Jiao K, Li X. Three-dimensional multiphase modeling of cold start processes in polymer electrolyte membrane fuel cells. Electrochimica Acta 2009;54:6876–91.
[31] Ye Q, Nguyen T. Three-dimensional simulation of liquid water distribution in a PEMFC with experimentally measured capillary functions. Journal of the Electrochemical Society 2007;154:B1242–51.

[32] Darling R, Meyers J. Kinetic model of platinum dissolution in PEMFCs. Journal of the Electrochemical Society 2003;150: A1523–7.
[33] Darling R, Meyers J. Mathematical model of platinum movement in PEM fuel cells. Journal of the Electrochemical Society 2005;152:A242–7.
[34] Wang Y, Wang C-Y. Modeling polymer electrolyte fuel cells with large density and velocity changes. Journal of the Electrochemical Society 2005;152:A445–53.
[35] Borutzky W, Barnard B, Thoma J. An orifice flow model for laminar and turbulent conditions. Simulation Modeling Practice and Theory 2002;10:141–52.
[36] Wu J, Yuan XZ, Martina JJ, Wang H, Zhang J, Shen J, et al. A review of PEM fuel cell durability: degradation mechanisms and mitigation strategies. Journal of Power Sources 2008;184: 104–19.
[37] Amundson NR, Pan T-W, Paulsen VI. Diffusion with Stefan and Maxwell. AIChE Journal 2003;49:813–30.
[38] Franco AA, Gerard M. Multiscale model of carbon corrosion in a PEFC: coupling with electrocatalysis and impact on performance degradation. Journal of the Electrochemical Society 2008;155:B367–84.

Nomenclature

A: area, m^2
D: diffusivity/diameter, $m^2\ s^{-1}/m$
E: cell voltage, V
J: diffusive flux, mol $m^{-2}\ s^{-1}$
n: molar fraction
N_t: total gas flux, mol $m^{-2}\ s^{-1}$
P: pressure, Pa
Q: hydrogen amount, mole
r: reactive/crossover flux, mol $m^{-2}\ s^{-1}$
R: gas constant, J K^{-1} mol^{-1}
s: liquid volume fraction
t: time, s/h
T: temperature, K
V: metal potential, V
W: volumetric flow rate, $m^3\ s^{-1}$

Greek

λ: membrane water content
ϕ: membrane potential, V
ν: kinematic viscosity, $m^2\ s^{-1}$
μ: dynamic viscosity, Pa s
ρ: density, kg m^{-3}
η: efficiency

Short-handed

AN: anode
CA: cathode
CH: flow channel
GDL: gas diffusion layer
Ctl: catalyst layer
Mem: membrane
sat: saturation

Subscript

V: vapor
N_2: nitrogen
H_2: hydrogen
O_2: oxygen
C: carbon
w: water